On pressure modes in ice-induced vibrations using multivariate analysis

Gedikli, Ersegun Deniz; Nord, Torodd Skjerve; Hendrikse, Hayo; Ziemer, Gesa

DOI
10.1016/j.coldregions.2019.02.003

Publication date
2019

Document Version
Final published version

Published in
Cold Regions Science and Technology

Citation (APA)
Gedikli, E. D., Nord, T. S., Hendrikse, H., & Ziemer, G. (2019). On pressure modes in ice-induced vibrations using multivariate analysis. *Cold Regions Science and Technology*, *160*, 150-162. https://doi.org/10.1016/j.coldregions.2019.02.003

Cold Regions Science and Technology 160 (2019) 150–162

Contents lists available at ScienceDirect

Cold Regions Science and Technology

journal homepage: www.elsevier.com/locate/coldregions

On pressure modes in ice-induced vibrations using multivariate analysis

Ersegun Deniz Gedikli[a,*], Torodd Skjerve Nord[a], Hayo Hendrikse[b], Gesa Ziemer[c]

[a] Sustainable Arctic Marine and Coastal Technology (SAMCoT), Centre for Research-based Innovation (CRI), Norwegian University of Science and Technology (NTNU), Trondheim, Norway
[b] Delft University of Technology, Delft, The Netherlands
[c] HSVA, Hamburg, Germany

ARTICLE INFO

Keywords:
Ice-induced vibrations
Ice-structure interaction
Pressure distribution
Proper orthogonal decomposition
Inexact robust principal component analysis

ABSTRACT

Pressures at the ice-structure interface during model-scale ice-structure interaction are often measured with tactile sensors. Resulting datasets usually include large volume of data along with some measurement error and noise; therefore, it is inherently hard to extract the hidden fluctuating pressures in the system. Identifying the deterministic pressure fluctuation in ice-induced vibrations is essential to understand this complex phenomenon better. In this paper, we discuss the use of two different multivariate analysis techniques to decompose an ensemble of measured pressure data into spatiotemporal modes that gives insights into pressure distributions in ice-induced vibrations. In particular, we use proper-orthogonal decomposition (POD) and inexact robust principal component analysis (IRPCA) in conjunction with measurements of intermittent crushing at different ice speeds. Both decompositions show that most of the energy is captured in a ten-dimensional space; however, the corresponding eigenvalues are different between the decompositions. While POD-based modes have low energy contributions at the first subspace dimensions, IRPCA-based modes have larger energy contributions. This result is consistent with the reconstruction of the time history of the pressure sum using first three empirical modes, where POD and IRPCA-based modes yield similar accuracy at the same subspace dimension. Although both methods successfully illustrate the dominant pressure modes that are active in the system, IRPCA method is found to be more effective than POD in terms of differentiating the contribution of each mode because of its ability to better separate low-rank and sparse components (measurement error and/or noise) in the dataset.

1. Introduction

Ice-induced vibrations (IIV) can be described as resulting motions of vertically sided offshore structures interacting with moving ice. Of particular interest, offshore structures in the Arctic and Subarctic regions may interact with the ice (i.e. level ice, deformed ice etc.) which might result in severe vibrations. This type of interaction may decrease the operational time significantly and may give fatigue related damages to the structures.

IIV first reported in the work of Blenkarn (1970) where full-scale observations of different structures in Cook Inlet, Alaska have been made. Later, many efforts have been made to understand such complex interactions through laboratory model tests (i.e. Barker et al., 2005; Kärnä et al., 2003, 2003b; Määttänen et al., 2012; Nord et al., 2015; Sodhi, 2001; Wells et al., 2011) and field campaigns (i.e. Bjerkås et al., 2013; Frederking et al., 1986; Määttänen, 1975).

Since the late 1990s, pressure sensors were implemented in the experimental setups to address the shape of pressure distribution at the ice-structure interface. Soon later, tactile sensors became the most commonly used instrument to measure the pressure distribution (Määttänen et al., 2011; Sodhi, 2001) and high-pressure zones (HPZ) (O'Rourke et al., 2016a, 2016b; Wells et al., 2011). The latter used the tactile sensor to address the influence of HPZs on the ice adjacent to indenter, and further how the HPZ influence the structural response. In addition to the use of pressure sensors, studies related to the ice fracture and contact shape were carried out through the use of plexiglass (Gagnon, 1994) and lexan plates (Joensuu and Riska, 1988). See Jordaan (2001) for a review of how the ice undergoes macroscopic changes during ice-structure interaction.

Tactile sensors are capable of displaying the pressure variation frame by frame and it allows observing the pressure change during a cycle of load build-up and ice failure. Global forces derived from the sensor can also be compared to the global forces measured by other means of instrumentation. Correlation coefficients between local forces measured by the tactile sensors were further used to describe the characteristics of the interaction during crushing at various ice speeds

* Corresponding author.
E-mail address: deniz.gedikli@ntnu.no (E.D. Gedikli).

https://doi.org/10.1016/j.coldregions.2019.02.003
Received 9 April 2018; Received in revised form 22 October 2018; Accepted 8 February 2019
Available online 13 February 2019
0165-232X/

(Sodhi, 2001). Sodhi and Haehnel (2003) showed that at low indentation speeds on a flexible structure, local pressures on the structure simultaneously increase to a uniform pressure distribution due to ductile (creep) deformation. As the indentation speed increased, cycles of saw-tooth force and displacement occur. During each cycle, the advancing ice sheet forces the structure to deflect and ductile deformation of the ice occurs until the terminal failure. At this point, the structure sways back due to release of strain energy and the relative speed between ice and structure increases causing a brittle type of failure with non-simultaneous contact. This mode of interaction is called intermittent crushing.

On a multi-degree of freedom structure, Nord et al. (2015) used Kalman type filtering techniques to show how the global response of the structure effected the pressure at the ice-structure interface during intermittent crushing. They showed that the superstructure oscillations caused the cyclic loading of the ice edge prior to the terminal failure, where high-frequency oscillations were superimposed to the saw-tooth.

Tactile sensors used in the laboratory experiments and field studies contain large amounts of information, which characteristically makes it difficult to analyze frame by frame. In addition, analyzing large datasets easily becomes time-consuming and comes at large computational costs. Therefore, reduced-order modeling (ROM) of such large datasets becomes essential where it can be used to unburden the redundant computations. Successful low-dimensional representation of high-dimensional data also enhance our understanding of complex dynamical systems where it helps to discover hidden fluctuating phenomena within the system.

Recent findings related to the pressure variations in the ice structure interface illustrate that there might be systematic structure hidden in the fluctuations that may enhance our understanding of ice-structure interactions (Määttänen et al., 2011; Wells et al., 2011). However, without extracting the dynamic modes and capturing the underlying physical mechanism with fewer degrees of freedom, we cannot find the coherent features in the dataset hence we are obliged to use all the data. Therefore, the goal of this study is to answer the scientific question: “Are there coherent pressure distributions exist at the ice-structure interface? Moreover, can we effectively identify these distributions? In addition, if such distributions exist, what would be the relationship between these dynamic modes and the motion of the structure?” To answer these questions, we use a statistical method called proper orthogonal decomposition (POD) and inexact robust principal component analysis (IRPCA) which is strongly related to the POD.

POD is a mathematical matrix decomposition method, which is best known to analyze complex flow phenomenon (Berkooz et al., 1993; Epps and Techet, 2010 and many more). It has been shown that it can successfully find the coherent structures hidden in the system using significantly fewer degrees of freedom and has been extensively used to find the most energetic contributions of the decomposed modes in the system with a least-squares sense. Therefore, it is an effective method not only for compressing the data but also with additional capabilities to summarize them. The method is closely related to singular value decomposition (SVD) (Epps and Techet, 2010), and it is also known as principal component analysis (PCA) and Karhunen-Loève decomposition in different research areas such as image processing and pattern recognition.

The most important characteristic of the POD method is that it fits the best ellipsoid to a given data in least squares sense (in $\mathscr{L}_2$-norm) and finds the optimal orthonormal bases that describe the data best. However, the method is not without limits. For example, if there are measurement errors embedded in the data, or if large noise fluctuations exist in the data, this method will inherently square the error in the analysis due to least-square fitting that may cause misleading results. It has been recently proposed by Candes et al. (2011) that instead of using $\mathscr{L}_2$-norm for data fitting, one can use $\mathscr{L}_1$-norm that promotes sparsity. Since the proposed new method also provides a certain level of robustness, it is called robust-principal component analysis (RPCA). The main idea of the RPCA method is that it allows separating the low-rank data and sparse components where sparse components represent the possible measurement errors and/or noise embedded in the system, and low-rank data represents the new data that has been separated from the sparse components. Later, Lin et al. (2013) further developed this method with a new proposed algorithm (so-called inexact robust principal component or IRPCA) using augmented Lagrange multipliers that solves the RPCA method much faster.

The approach used in this work resembles to the approach that has generally been used in the experimental fluid mechanics community (Berkooz et al., 1993; Epps and Techet, 2010) where POD has been used to analyze particle image velocimetry (PIV) data. However, in the present study, we not only apply traditional POD method to a three-dimensional pressure dataset, we also apply IRPCA algorithm as an advanced treatment to the POD problem. As a result, we reveal the organized patterns within the pressure data during intermittent crushing, which we name as pressure modes throughout the paper.

2. Proper-orthogonal decomposition

As briefly described above, POD is a mathematical matrix decomposition method that helps to characterize the coherent structures in a dataset. It has been used in almost all engineering fields where it is widely used for modal analysis, modal order reduction and characterization of both linear and non-linear systems (Berkooz et al., 1993; Feeny and Kappagantu, 1998; Gedikli et al., 2017; Gedikli and Dahl, 2017; Kerschen et al., 2005; Ma et al., 2001). Although POD is a linear approach, it is also applied to the nonlinear problems since it does not violate the physical laws of linearization methods as shown in Berkooz et al. (1993). However, it should be remembered that if the system is strongly nonlinear, even small changes in the initial conditions might affect the resulting dynamical behavior and the stability of the system. Therefore, the treatment proposed here is merely the first step taken analyzing these large datasets related to ice-induced vibrations and obtaining a ROM representation.

2.1. POD formulation

Let $\boldsymbol{D}$ be $m \times n$ zero mean data matrix, where m represents snapshots and n represents position state variables. In POD, we are looking for base functions $\boldsymbol{p}_n(t)$ and $\boldsymbol{\chi}_n(x)$, which describe the original data matrix best in least squares sense.

The data matrix can be written as:

$$\boldsymbol{D}(x,t) = \sum_{n=1}^{\infty} \boldsymbol{p}_n(t)\boldsymbol{\chi}_n(x) \tag{1}$$

where $\boldsymbol{D}(x,t) \in \mathbb{R}^{m\times n}$, and $\boldsymbol{\chi}_n(x)$ represents the orthonormal basis functions (modes) and $\boldsymbol{p}_n(t)$ represents corresponding time coordinates. A detailed derivation of this method can be found in many studies (i.e. Berkooz et al., 1993; Cruz et al., 2005).

Geometrically, a scalar field sampled in time can be imagined as a cloud of points in a n-dimensional space, where n is the number of spatial sampling points. In this space, POD fits the best ellipsoid to this cloud of points in the least squares sense where the directions of semi-principal axes give proper orthogonal modes (POM) and the squared magnitudes of the semi-principal axes correspond to the variance of the projection points on the subspace span by the corresponding axes and represent proper orthogonal values (POV). Therefore, POD provides energy optimal reduction in dimension.

In the current analyses, the dataset has a three-dimensional structure where pressure fluctuates in a two-dimensional space over time as sketched in Fig. 1. The evolution of the process is simple. When an ice sheet interacts with the structure, it forms pressures at the ice-structure interface, which depend on ice failure, ice properties, structural properties, and the relative speed between ice and the structure. Since there

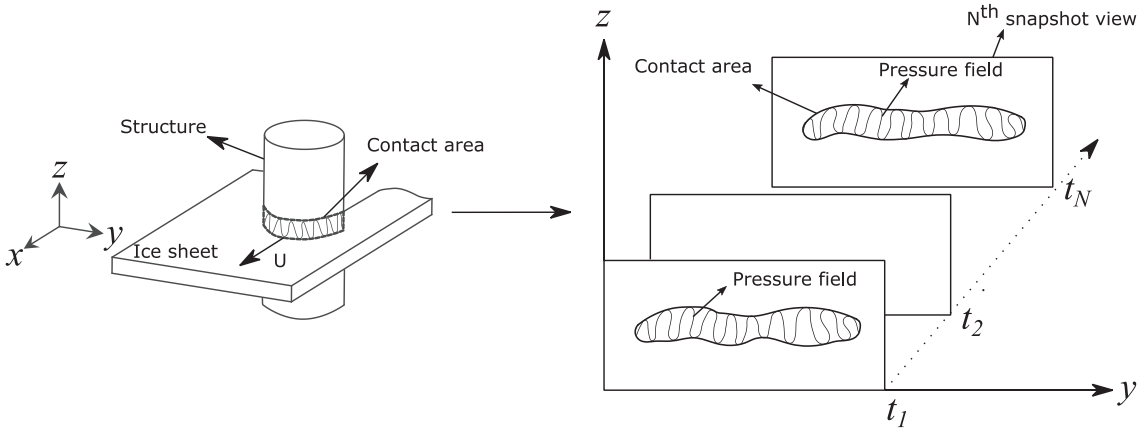

Fig. 1. Left image: Schematic of the ice-structure interaction (isometric view). Right image: Front view of the ice-structure interaction setup with varying pressure field as snapshot. Ice sheet is frozen and structure is moving in the *x*-direction (as in Test-4300) with ice speed of *U*.

are many coupled parameters that might affect the interaction, this process is not fully understood. Of particular interest, pressure zones may fluctuate in ice drift direction, may move up and down (in the thickness of the ice) and may vary across the circumference of the structure with varying amplitudes during the ice-structure interaction. Therefore, it is a valid assumption that pressure varies not only in the *yz* phase as shown in the schematic of the ice-structure interaction in Fig. 1, but it may also vary in the ice drift direction (in *xy* phase).

Suppose that pressure variation has the form of $\boldsymbol{d} = [y, z]$ in a two-dimensional space. So, fluctuating pressure components of the snapshots can be written as one data matrix as; $\boldsymbol{D} = [\boldsymbol{d_1 d_2 \cdots d_N}]$. In other words, each snapshot of pressure fluctuations has been reorganized and arranged into two-dimensional $M \times N$ data matrix where *M*'s size is equal to the size of $y \times z$, and *N*'s size is equal to number of snapshots.

Since, in traditional POD analysis the eigenvalue of the auto-covariance matrix is solved, the auto-covariance matrix can be calculated as:

$$\boldsymbol{A} = \boldsymbol{D}^T \boldsymbol{D} \tag{2}$$

Where superscript *T* represents transpose.

Next, one can solve the eigenvalue problem of **A** as:

$$\boldsymbol{A V}_i = \lambda_i \boldsymbol{V}_i,\ i = 1, 2, \ldots, \boldsymbol{N} \tag{3}$$

where $\boldsymbol{V}$ represents the eigenvector matrix, and λ represents the corresponding eigenvalues. Then, eigenvalues and corresponding eigenvectors are sorted in descending order. This step is very important because, it allows sorting the modes where most dominant (coherent) structures will be in the first subspace dimensions.

Then, projecting the eigenvectors onto the data matrix and normalizing them to unit magnitude gives the corresponding proper orthogonal modes (POMs). By reshaping the two-dimensional POM matrix back to the three-dimensional matrix, one can illustrate the coherent structures that are active in the system. Mathematically, any i^{th} POD mode of $\boldsymbol{\chi}_i$ may be found calculating the following equation:

$$\chi_i = \frac{\sum_{n=1}^{N} V_{i.n} \boldsymbol{d_n}}{\| \sum_{n=1}^{N} V_{i.n} \boldsymbol{d_n} \|},\ i = 1, 2, \ldots, \boldsymbol{N} \tag{4}$$

where $V_{i,\ n}$ represents the n^{th} eigenvector corresponding to i^{th} eigenvalue. Then, one can also compute the basis function of $\boldsymbol{p}_n(t)$ in Eq. (1) by projecting the pressure field onto the POMs (see Eq. (5)). This basis function is also known as proper orthogonal coordinates (POCs). Forming a POM matrix of $\boldsymbol{\phi} = [\boldsymbol{\chi}_1, \boldsymbol{\chi}_2, \boldsymbol{\chi}_3, \ldots, \boldsymbol{\chi}_N]$, one can calculate the POCs as:

$$\boldsymbol{p}_n = \boldsymbol{\phi}^T \boldsymbol{d}_n \tag{5}$$

Original data can be reconstructed using any first *N* POMs:

$$\boldsymbol{d}_n = \boldsymbol{\phi p_n} \tag{6}$$

One can also reconstruct the data using first *r* POMs (with rank *r* approximation where $r < N$) with certain level accuracy which may be decided based on the level of energy in the system using Eq. (8).

$$\boldsymbol{d}_r = \boldsymbol{\phi p_r} \tag{7}$$

Eigenvalues of the auto-covariance matrix are generally referred as energies corresponding to the POMs in fluid mechanics since it is related to fluid's kinetic energy (Chatterjee, 2000). Although, it is not attempted to relate the fluid characteristics to the pressure characteristics in this study, it is assumed that distributed pressure variations due to solid-structure interaction resemble to flow variations in fluid mechanics.

The quality of the reconstruction (mode energy) can theoretically be found using the eigenvalues in POD, or singular values in SVD (note that square of the singular values in SVD is mathematically equal to eigenvalues obtained from POD as shown in Chatterjee (2000)):

$$E_r\ [\%] = \frac{\sum_{n=1}^{r} \lambda_n}{\sum_{n=1}^{N} \lambda_n} \tag{8}$$

where *E* represents mode energy and *r* represents the rank of the system (number of modes used in the reconstruction). Solution to this equation gives the cumulative energy of modes up to mode number *r*. Alternative to the energy fraction, the eigenvalues can be sorted logarithmically where the difference between each mode can easily be seen on a logarithmic plot. Another way of comparing the quality of the reconstruction is the root-mean-square-error (RMSE) analysis where one can find the error between any desired rank and the original signal. Ideally, if the RMSE error with high probability close to the theoretical solution from the eigenvalues, that would be an ideal error bound. In this study, all three methods are used to illustrate how the energies associated with the pressure modes vary in different subspaces.

3. Robust principal component analysis (RPCA)

In the previous section, it is mentioned that, POD produces POMs using the auto-covariance matrix of the data where it fits the best ellipsoid to the clouds of points in the least squares sense ($\mathscr{L}_2$-norm). However, suppose data contains large outliers, then POD will result a large bias, which will shift the true fit to compensate the outliers in the system. However, Candes et al. (2011) showed that finding an $\mathscr{L}_1$-norm minimization solution to this data effectively rejects these outliers and increases the robustness of the best data fit. This is significant, because if the data is corrupted, or has large noise embedded in it, then POD algorithm will potentially square the error and give misleading results. In that sense, $\mathscr{L}_1$-norm minimization promotes sparsity as illustrated in

compressive sensing applications (Candes and Wakin, 2008).

Let use $\boldsymbol{D}$ again as the original data matrix. Candes et al. (2011) suggests that the original data matrix can be decomposed into two components as low-rank (L) and sparse (S) through the use of tractable convex optimization. In other words, the data matrix can be written as:

$$\boldsymbol{D} = \boldsymbol{L} + \boldsymbol{S} \tag{9}$$

Then, the problem becomes a convex optimization problem as follows:

$$\min_{L,S} \|\boldsymbol{L}\|_* + \lambda \|\boldsymbol{S}\|_1, \text{ subject to } Eq.\ (9) \tag{10}$$

where $\|\boldsymbol{L}\|_*$ represents the nuclear norm of the low-rank ($\boldsymbol{L}$) matrix, or in other words sum of the singular values of the $\boldsymbol{L}$ matrix, $\|\boldsymbol{S}\|_1$represents the $\mathscr{L}_1$-norm of $\boldsymbol{S}$ and λ is regularizing parameter. In this study, λ is fixed to $\lambda = 1/\sqrt{m}$, where m has the same size of the auto-covariance matrix in Eq. (2) (Wright et al., 2009).

Later, Lin et al. (2013) have further improved this method and proposed an algorithm using Inexact-Augmented Lagrange Multipliers (IRPCA), which solves the convergence problem much faster with much higher precision. Although the details of this method is beyond the scope of this study, IRPCA algorithm proposed by Lin et al. (2013) is also used in this study as an advanced treatment to POD. After separating the data into low-rank and sparse components, the low-rank component is further analyzed using traditional POD following the steps in Section 2 and new pressure modes are obtained. To be consistent, the resulting mode shapes are also called POMs (or pressure modes) since this method can be thought as an advanced filtering technique rather than a complete new method. The significance of this particular method is that a perfect separation is always guaranteed as proved by Candes et al. (2011). In that sense, being able to separate the large data matrix into low-rank and sparse components does not only help to eliminate the large noise and experimental error in the system, but also enhance our understanding of complex ice-structure interactions.

4. Experiments

In the present study, experimental data obtained from the deciphering ice-induced vibration (DIIV) test campaign is used. The DIIV campaign was initiated by the Norwegian University of Science and Technology (NTNU) in the beginning of 2011 to understand the complex ice-induced vibrations through model-scale tests. The tests were conducted at the Hamburg ship model basin (HSVA) ice-tank facility in Hamburg, Germany. In the experiments, ice and structural parameters were systematically investigated in a well-defined test setup as described in Määttänen et al. (2012). The experimental set up is shown in Fig. 2, where the natural frequencies could be varied by changing stiffness and/or mass. The tactile sensor was installed to the 220-*mm*-diameter indenter and protected by a 0.5 *mm* thick aluminum film. This sensor had 52 columns and 44 rows of sensels, so that in total 2288 sensels measured pressures during ice-structure interaction.

4.1. Relevant data

From the DIIV campaign, Test 4300 is chosen for this study. The reason of it is that it is the only test in the campaign where the ice speed is investigated in a systematic manner (ice speed is varied stepwise). Table 1 shows the experimental test parameters and tested ice speeds with respect to their specific time range for Test 4300. Natural frequency values of 12.2*Hz* and 16.1*Hz* in Table 1 represent the first and second mode frequencies of the structure.

Fig. 3 illustrates the specific time characteristics of the Test 4300 where the top image (Fig. 3a) represents the time history of the sum of the force; center image (Fig. 3b) represents the corresponding frequency variation of the strain gauge response and the bottom image (Fig. 3c) represents the ice speed range over time where ice speed is increased in steps. As one can see, sum of all the measured forces due to ice-structure interaction varies around 10*kN* between 30 and 320*s* with different frequencies.

Of particular interest, ice speeds of 20,30,40,50,60,70 $mm\ s^{-1}$ are analyzed, where all of these ice speeds represent intermittent crushing and exhibit a dominant response frequency much less than the first natural frequency (first red line in Fig. 3b). It should also be noted that as the ice speed increases, the ice-structure interaction occurs faster and therefore both the resulting frequency and randomness in the data increases. More details on the force and response characteristics of this particular test can be found in Nord et al. (2015).

5. Results

In the analysis, zero-mean pressure responses are obtained using a Butterworth high-pass filter with 1 *Hz* cut-off frequency. The cut-off frequency is chosen based on the visual inspection of the frequency response so that it is sufficient to cancel the zero frequencies, but retain the dominant frequency of the ice force. However, it should be remembered that zero-mean pressure response presented here could simply be obtained by removing the centered moving average from the original data as well, which yields similar results in the current experiments (not shown). Therefore, in this analysis technique, zero-mean response is attributed to the dynamic pressure variations and mean component is attributed to the static pressure on the structure.

In ice-structure interaction, ice can behave ductile and brittle depending on the relative indentation speed between ice and structure; therefore, the load build-up and unloading phase become different during intermittent crushing. During load build-up, the relative speed between the indenter and ice is close to zero, the contact area and pressure grow as a result of the ductile deformation of the ice. Upon ice fracture, the relative speed between ice and structure increases with orders of magnitude, and causes brittle ice failure hence a sharp load drop.

In this work, seven different time series of intermittent crushing are analyzed between the ice speeds of 20 and 70 $mm\ s^{-1}$. However, only the results at 30 and 60 $mm\ s^{-1}$ are presented here for clarity and rest of them are tabulated in Table 2. In addition, an extra time series of intermittent crushing is analyzed from IVOS (Ice-induced Vibrations of Offshore Structures) Phase 2 test campaign for comparison because the new time series has a much higher sampling rate with the value of 300*Hz* and longer time history of 75*s* than the tests in DIIV test campaign. Detailed information regarding relevant analysis is presented at the end of the Results section of this paper but readers are encouraged to read Ziemer and Hinse (2017) for detailed information about IVOS test campaign.

5.1. Pressure modes of intermittent crushing at ice speed of 30 mm s^{-1}

Fig. 4 illustrates the original and high-pass filtered time histories of the pressure sums on the structure. As one can clearly see, the applied filter successfully removes the mean to zero value to identify the dynamic variations. As a result of this filtering process, the resulting time history is not get affected by the filtering and both responses demonstrate a clear saw-tooth type of response within the time range selected.

Fig. 5 shows the mode shape characteristics (pressure modes) and their relative contributions due to ice structure interaction at the ice speed of 30 $mm\ s^{-1}$ using POD (Fig. 5a) and IRPCA (Fig. 5b) methods. Left images in Fig. 5 illustrate the eigenvalues of the first 10 subspaces whereas center and right images illustrate the corresponding POMs of the first six subspaces. The distribution of the eigenvalues shows that the first eigenvalue is significantly larger than the second and the second eigenvalue is larger than the third and so on. Since, POD sorts the modes based on their energies in the descending order, it means that POM in the first subspace represents the most dominant mode;

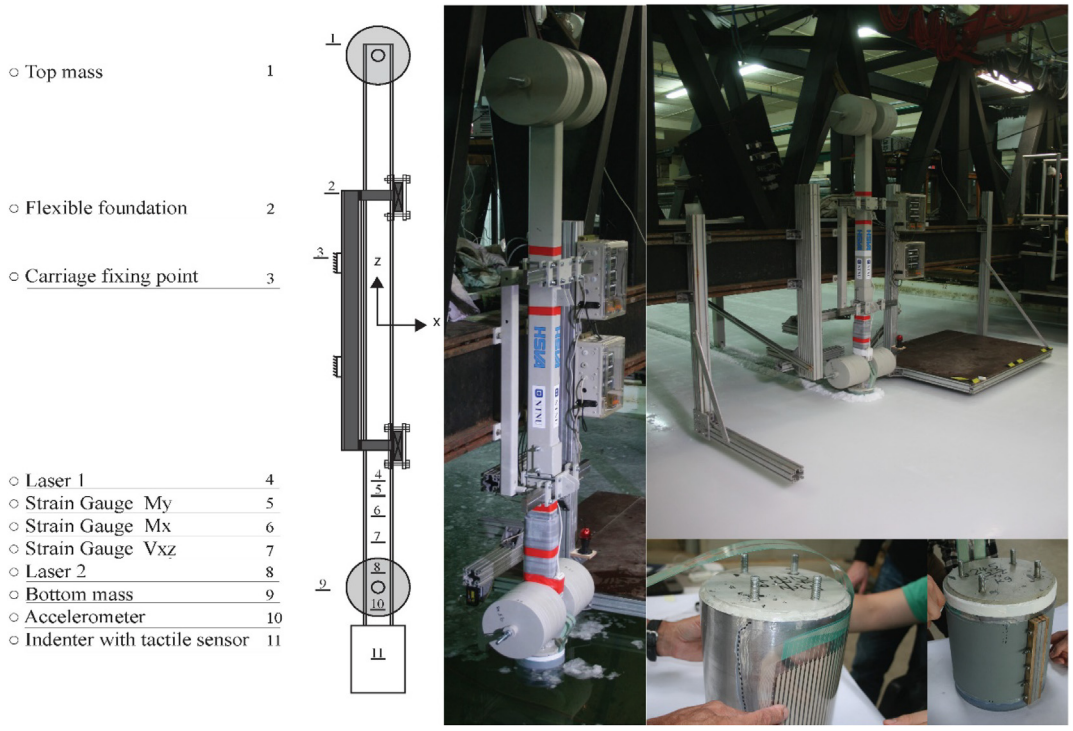

Fig. 2. Experimental setup showing the sensor locations (left sketch), the test structure (center and top-right images) during ice-structure interaction along with the tactile sensor installation on the indenter (right bottom image).

Table 1
(a) Experimental test matrix. **(b)** ice speed with respect to a specific time range for comparison.

(a) Test-4300	
f_n (*Hz*)	12.2 and 16.1
Diameter (*mm*)	220
Ice speed ($mm\ s^{-1}$)	10 − 320, Spacing = 10 & 20
Analyzed ice speed ($mm\ s^{-1}$)	20 − 70, Spacing = 10
Sampling frequency (*Hz*)	100
Ice thickness (mm)	60
Ice temperature (°C)	−1.7
Ice salinity (ppt)	3.2

(b) Ice-speed vs Time (s)						
Speed ($mm\ s^{-1}$)	20	30	40	50	60	70
Time (s)	65–80	85–100	105–115	120–130	135–145	147–157

POM in the second subspace dimension represents the second most dominant mode and so on.

Both multivariate analysis approaches reveal that the pressure distribution has a line shape on the structure in the first subspace dimension as expected. This pressure mode represents the most dominant distribution and representative of the ductile load build-up on the structure. As the subspace dimension increases, the contribution of the higher order modes decreases. The second POM shows that there is one high-pressure zone displayed in yellow and one line of pressure displayed in blue colour, which resembles to a standing wave type of response (the peaks of the oscillation does not change spatially). If one reconstructs the pressure using only the second POM, one can clearly see that the colour of the pressure zones (blue and yellow) switches in time, which illustrates the dynamic variation of the second POM. The yellow pressure zone is almost symmetric across the circumference of the structure in the second POM, whereas the blue pressure zone is not, which is believed to result in sideway motions of the structure for the reasons that will become apparent later. Higher order modes (higher

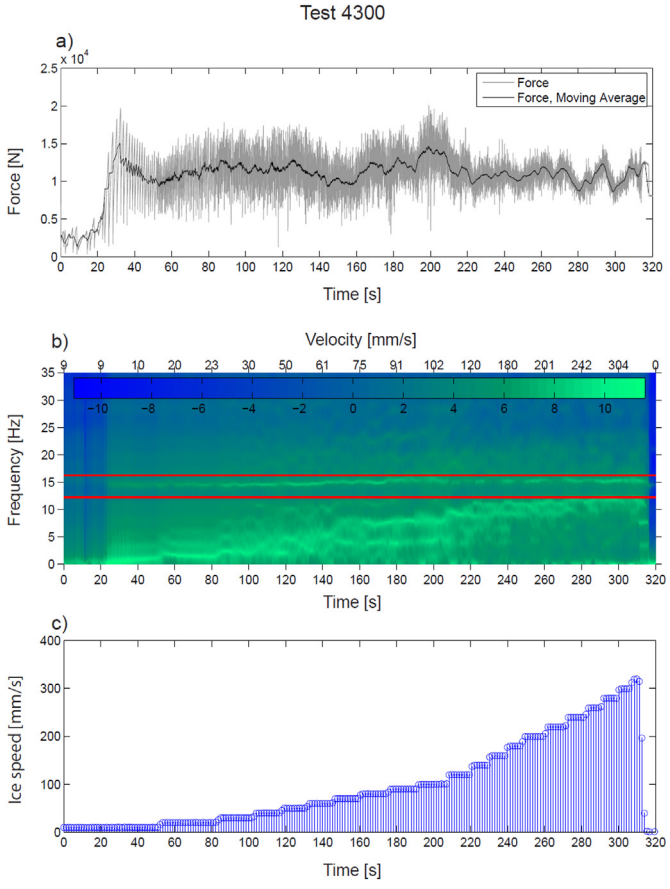

Fig. 3. (a) Time history of the force, (b) frequency variation with respect to time, and (c) ice speed range for Test 4300 (from Nord et al. (2015)).

Table 2
NRMSE of the rank-3 approximation and modal energies for low-rank approximations of the matrices **L** and **A** for IRPCA and POD, respectively.

Ice speed [mm s^{-1}]	20	30	40	50	60	70
$\lambda = 1/\sqrt{m}$	0.021	0.021	0.021	0.021	0.021	0.021
NRMSE [%] POD ($r = 3$)	2.7	3.3	3.9	4.4	6.9	6.6
NRMSE [%] IRPCA ($r = 3$)	3.4	3.9	5.3	5.5	8.8	10.5
POD E [%] of **A**						
Rank 1	34	22	14	11	11	8
Rank 2	44	31	25	20	19	15
Rank 3	49	38	34	28	25	22
Rank 10	72	66	64	58	52	48
Rank 20	86	81	76	77	72	68
Rank 50	96	94	95	93	90	89
IRPCA E [%] of **L**						
Rank 1	49	31	23	18	23	19
Rank 2	59	43	37	33	38	34
Rank 3	66	53	50	44	47	47
Rank 10	88	84	85	80	82	81
Rank 20	97	95	98	96	96	95
Rank 50	99.9	99.9	99.9	99.9	99.9	99.9

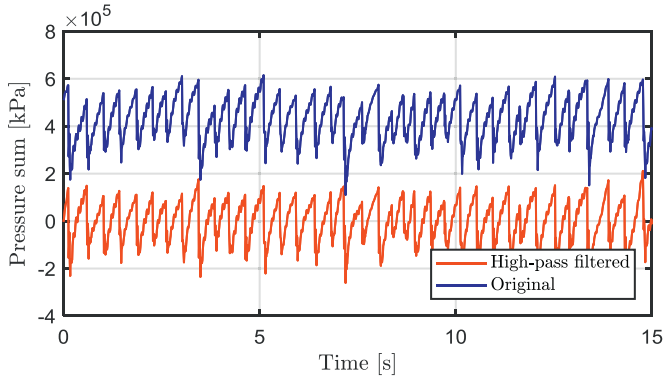

Fig. 4. Time-history plots of sum of tactile sensor pressures at ice speed of 30 *mm s*$^{-1}$, original response (blue, top) and high-pass filtered response (red, bottom). (For interpretation of the references to colour in this figure legend, the reader is referred to the web version of this article.)

than second pressure mode) illustrate different type of responses (travelling, standing and complex); however, because their individual contributions are low, their effect on the structure is negligible (see Table 2).

Another important observation is that, POMs of POD and IRPCA resemble to each other; however, there is a significant difference in the corresponding eigenvalues. In POD, eigenvalues of the higher order modes are close one another which results low energy contributions at low subspace dimensions. This solution also contradicts the normalized root-mean-squared-error (NRMSE) analysis of the rank-3 approximations as shown in Fig. 6. However, in IRPCA, eigenvalues are better separated from one another, which yields larger energy contributions at low subspace dimensions.

Fig. 6 shows the original and reconstructed time signals using first three POMs obtained from IRPCA algorithm (see Table 2 for POD). NRMSE is computed between the original and reconstructed signals, where the resulting solution is also normalized with the maximum variation in amplitude in the original data. As a result, one can see that rank-3 approximation of the sum of the pressure at ice speed of 30 *mm s*$^{-1}$ results in good accuracy with the NRMSE value of 0.039 (3.9% error). This result is important because it validates how well the reduced order model can represent the original data where rank-3 approximation to the problem not only captures the dominant frequency of ice failure, but also the higher frequency components that are caused by superstructure oscillations as described in Nord et al. (2015).

One can also see the relationship between the pressure modes and the structural responses by comparing their frequencies. Left three images in Fig. 7 illustrate the frequencies of the first three pressure modes and right image represents the structural frequencies in ice-drift (right-top) and sideway (right-bottom) directions. Fig. 7 clearly shows that first POC frequency is equal to the structural frequency in the ice-drift direction. This is in agreement with our explanation to the problem where first pressure mode represents the most dominant mode. More interestingly, second and third POC frequencies are equal to the structural vibrations in the sideways direction, which means that some combination of second and third modes are representative of the pressure distribution in that direction. Since second pressure mode has more energy than the third pressure mode, it can be related to the pressure zone in the circumference of the structure, which causes sideways vibrations.

In addition, second and higher-pressure modes also capture the pressure variations in the structural depth/ ice thickness direction (shown as z-direction in Fig. 1). The motion in ice thickness direction is also observed when playing the video of the tactile sensor pressures frame by frame. Higher modes (higher than third pressure mode) contain dominant frequencies that coincide with the cross-flow response frequencies (not shown), but the slow decay of the eigenvalues and also the resulting mode shapes suggest that they are linear combinations of first three POMs.

5.2. Pressure modes of intermittent crushing at ice speed of 60 mm s^{-1}

Fig. 8 illustrates the original and high-pass filtered time histories of the pressure sums on the structure at the ice speed of 60 *mm s*$^{-1}$. Similar to previous case, the applied filter successfully removes the mean to zero value to identify the dynamic variations at this ice speed and the resulting shape resembles to a saw-tooth type of response. It is observed that intermittent crushing at this ice speed occurs with an apparent dominant force frequency and resulting response frequency is lower than the natural frequency (see Fig. 3).

Fig. 9 illustrates the pressure modes and their relative contributions due to ice structure interaction at the ice speed of 60 *mm s*$^{-1}$ using POD (Fig. 9a) and IRPCA (Fig. 9b) methods. Left images in Fig. 9 show the logarithmic plot of the eigenvalues of the first ten-subspace dimensions, and center and right images represent the corresponding pressure modes of the first six-subspace dimensions. The distribution of the eigenvalues in Fig. 9a shows that the relative contribution of the first two pressure modes are significantly larger than the higher subspace dimensions and there is no significant difference in the relative contribution of the higher order modes which results low energy contributions of the first subspace dimensions. This condition is similar to the observations from the ice speed of 30 *mm s*$^{-1}$. However, when the IRPCA method is applied (Fig. 9b), it is once again observed that the eigenvalues are better separated and resulting modes shapes are not affected from this analysis.

Similarly, both multivariate analysis approaches reveal that the pressure distribution has a line shape on the structure in the first subspace dimension as expected. This pressure mode represents the most dominant pressure distribution and representative of the load build-up on the structure. Large second eigenvalue suggests that second pressure mode also contributes to the dynamic process significantly where the resulting pressure mode resembles to a travelling wave type of response (maximum and minimum pressure values travel spatially). Higher order modes (higher than second pressure mode) illustrate different type of responses (travelling and/or complex); however, because their contribution is low, their effect on the structure is negligible (see Table 2).

Fig. 10 shows the original and reconstructed signals using first three POMs obtained from IRPCA algorithm (see Table 2 for POD). As a result, one can see that rank-3 approximation of the sum of the pressure at ice speed of 60 *mm s*$^{-1}$ results very good accuracy with the NRMSE value of 0.087 (8.7% error).

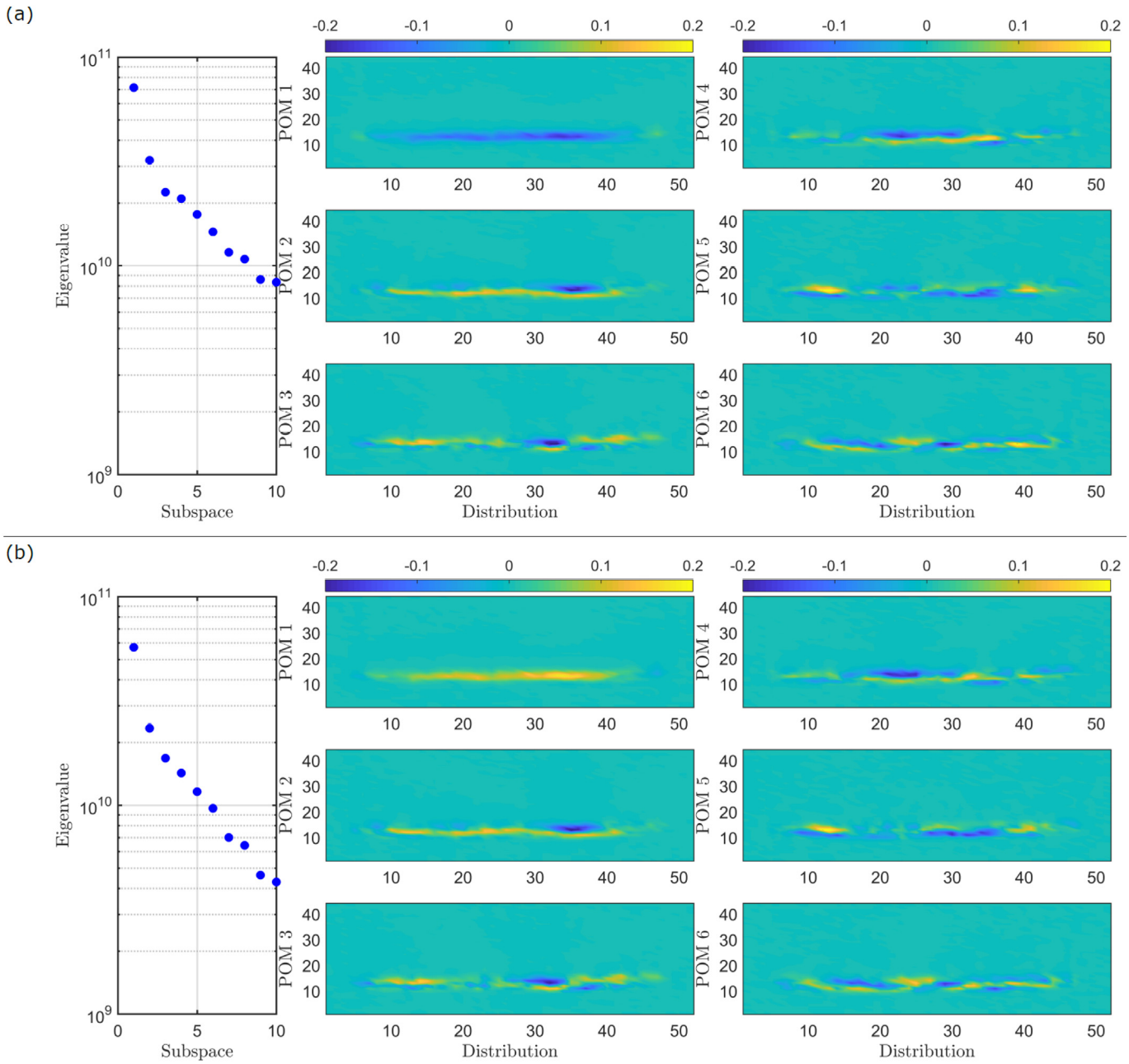

Fig. 5. Top image (a): Logarithmic plot of eigenvalues (left image) and corresponding six pressure modes (center and right images) at 30 $mm\,s^{-1}$ ice speed using POD. Bottom image (b): Logarithmic plot of eigenvalues (left image) and corresponding six pressure modes (center and right images) at 30 $mm\,s^{-1}$ ice speed using IRPCA.

One can also compare the frequencies of the decomposed modes with the structural frequencies to illustrate the relationship between the pressure modes and the structure. As a result, dominant frequencies of the first two POCs (Figs. 11a-b) coincide mostly with the frequency of structural response in the ice-drift direction (Fig. 11d) and the third POC (Fig. 11c) has a dominant frequency coincides with the structural response in the sideway direction (Fig. 11e). This is different from the ones that has been observed in the previous section. There, the frequency of the first pressure mode is equal to the frequency in the ice drift direction and the frequency of the second and third modes are equal to the structural frequency in the sideways direction. However, at this flow speed it is observed that first and second pressure modes coincide with the frequency in the ice drift direction which means that some combination of these modes better represent the most dominant pressure mode that is active in this direction of the motion. This is a significant finding because it clearly illustrates the nonlinear nature of the coupled in-line (ice drift) and cross-flow (sideways) motions. In this case, the effect of higher order modes also seems insignificant in comparison with the first two modes. Distribution of the eigenvalues (slow decay) and the corresponding mode shapes also support this phenomenological analysis.

It should be noted that, this decomposition and error analysis are performed for only the ice speeds between 20 and 70 $mm\ s^{-1}$. The reason of is that at the lower ice speeds the process is more periodic and clear than the interactions at higher speeds, at which continuous brittle crushing governs the interaction. It is therefore easier to connect the decomposed modes to structural vibrations. However, it is expected that the error between the reconstruction and the original signal will increase as the method is applied to higher drift speeds due to the increase in the randomness of the process. In fact, NRMSE of the rank-3 approximation in IRPCA increases from 3.4% to 10.5% gradually as the ice speed increased from 20 to 70 $mm\ s^{-1}$, as shown in Table 2. One

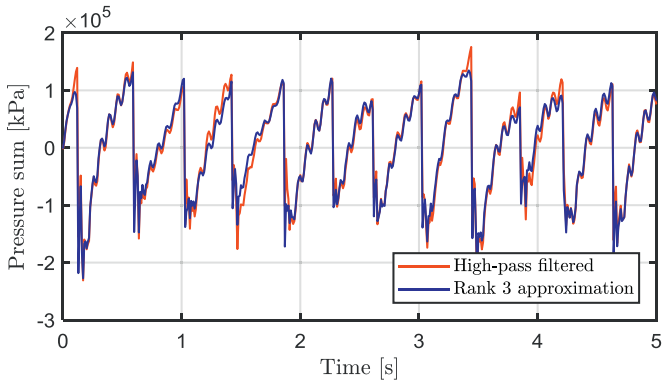

Fig. 6. Example time history of the sum of pressures for the original data (red) and rank-3 approximation (blue) at 30 $mm\ s^{-1}$ ice speed obtained using IRPCA algorithm. (For interpretation of the references to colour in this figure legend, the reader is referred to the web version of this article.)

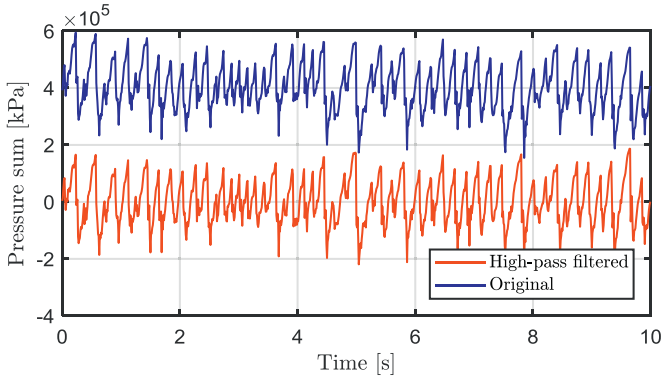

Fig. 8. Time-history plots of sum of tactile sensor pressures at ice speed of 60 $mm\ s^{-1}$, original response (blue, top) and high-pass filtered response (red, bottom). (For interpretation of the references to colour in this figure legend, the reader is referred to the web version of this article.)

reason for this is that as the ice speed increases, the number of time increments during load build-up becomes smaller whereas number of time increments during failure becomes larger. This happens because the dominant force frequency increases with increasing ice speed. It is questionable whether the tactile sensor response is fast enough to capture the higher frequencies inherent in the brittle failure, which may explain the increased reconstruction error with ice speed. In the analysis λ regulating parameter is kept constant using $\lambda = 1/\sqrt{m}$ where m is equal to the size of the auto-covariance matrix as suggested by Wright et al. (2009).

Another important characteristic of these reduced order models is that the choice of rank of a reduced-order representation of the data depends on the desired accuracy determined by the user of the method. Table 2 illustrates the NRMSE of rank-3 approximation using POD and IRPCA algorithms where r represents the rank of the system and the modal energy for different ranks according to Eq. (8).

5.3. *Pressure modes of intermittent crushing at ice speed of 5 mm s^{-1} from Test−22120 phase II in IVOS*

An extra time series of intermittent crushing is analyzed from IVOS (Ice-induced Vibrations of Offshore Structures) Phase 2 test campaign for comparison where the sampling rate is 300Hz and time length is around 75s (the sampling rate was around 100Hz in DIIV test campaign where the time length of individual ice speed was varying between $10 - 15s$).

In the tests, the test cylinder is mounted to the main carriage and moves through the resting ice sheet to get insight into dynamic ice-structure interaction. Tested cylinder has a diameter of 200 mm where the model is equipped with tactile sensors and a 6-component scale measures the global loads. Similar to the analysis followed for DIIV experiments; first, zero-mean response is obtained and then POD and IRPCA of the resulting data are computed. Table 3 shows the relevant test matrix and modal energies for different ranks according to Eq. (8). However, readers are encouraged to read Ziemer and Hinse (2017) for more detailed information regarding the IVOS test campaign.

Fig. 12 illustrates the zero-mean original data and rank-3 approximation of the pressure sums on the structure at the ice speed of 5 $mm\ s^{-1}$ when IRPCA method is used. NRMSE of the rank-3 approximation is calculated using both POD and IRPCA methods and found as 4%, 7 %, respectively.

Fig. 13 shows the pressure modes and their relative contributions due to ice structure interaction at the ice speed of 5 $mm\ s^{-1}$ using POD (Fig. 13a) and IRPCA (Fig. 13b) methods. Left images in Fig. 13 illustrate the eigenvalues of the first 10 subspaces whereas center and right images illustrate the corresponding POMs of the first six subspaces. The

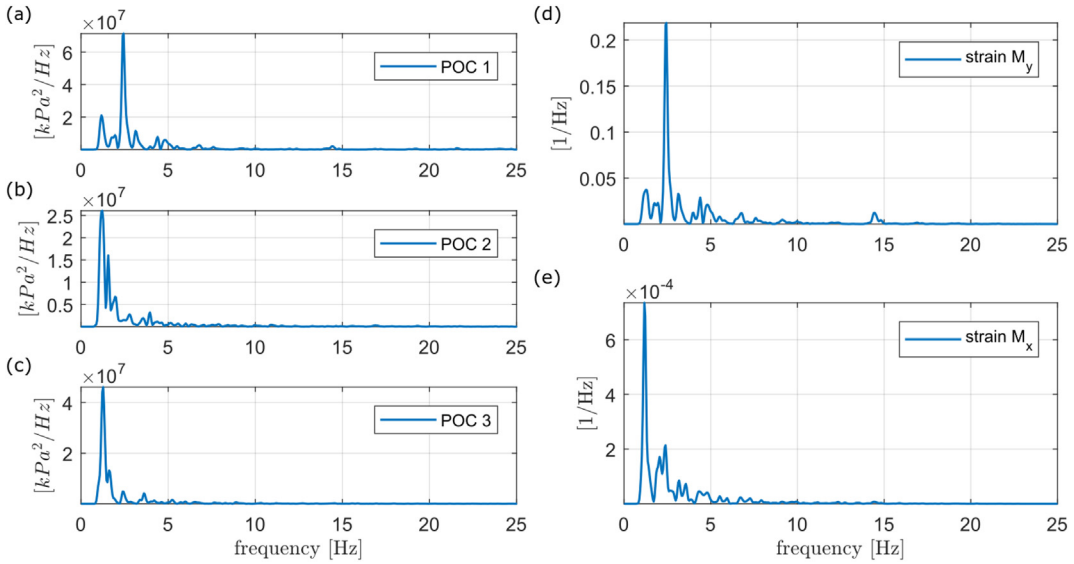

Fig. 7. Spectral densities of POD coefficients for the first three pressure modes (left) and spectral densities of strains due to ice action in the ice-drift direction (upper right) and sideways direction (lower right) at ice speed of 30 $mm\ s^{-1}$.

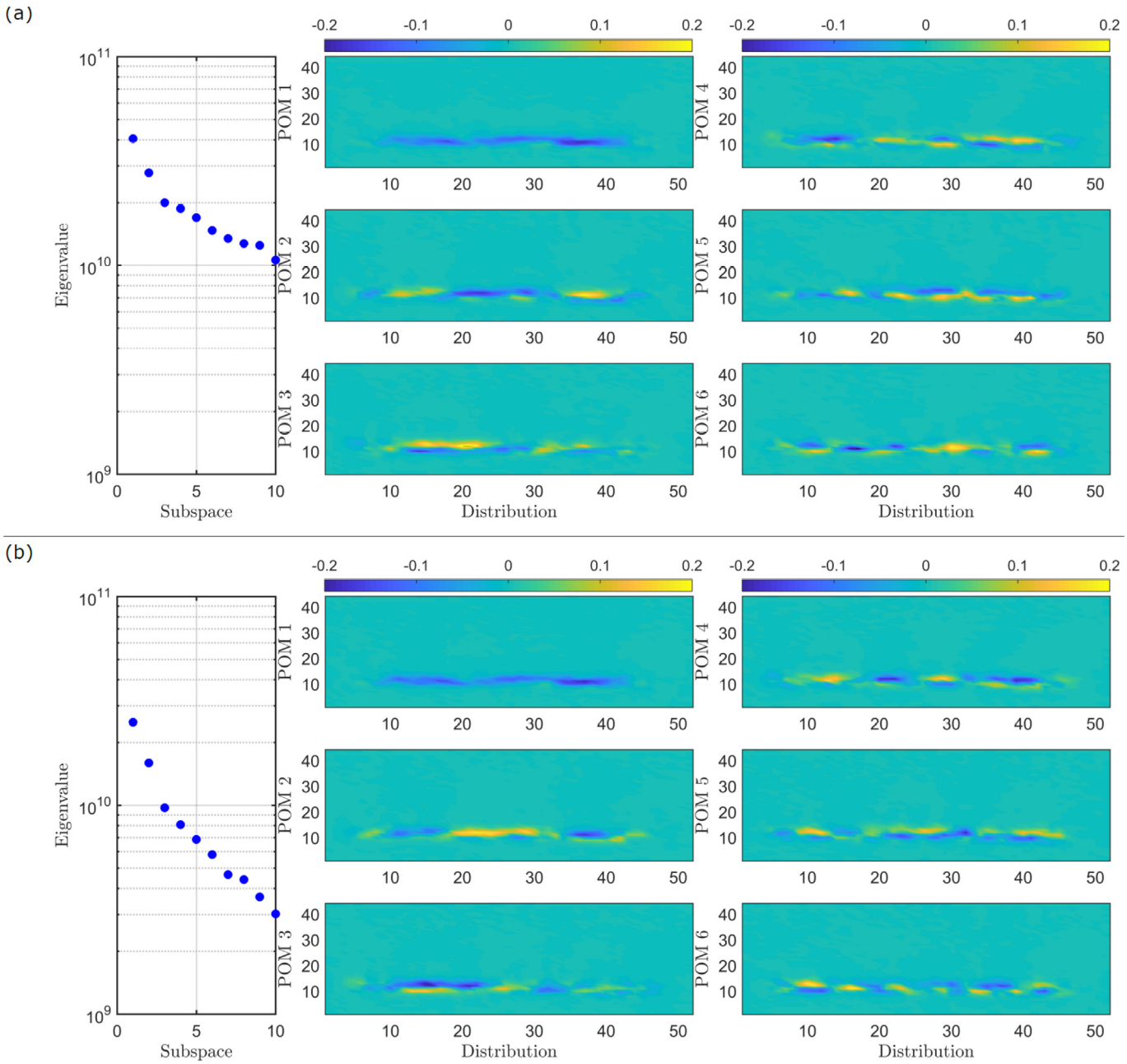

Fig. 9. Top image (a): Logarithmic plot of eigenvalues (left image) and corresponding six pressure modes (center and right images) at 60 $mm\,s^{-1}$ ice speed using POD. Bottom image (b): Logarithmic plot of eigenvalues (left image) and corresponding six pressure modes (center and right images) at 60 $mm\,s^{-1}$ ice speed using IRPCA.

distribution of the eigenvalues shows that the first two eigenvalues are significantly larger than higher order modes when regular POD method is used (Fig. 13a) and contribution of the higher modes become more apparent when IRPCA method is used (Fig. 13b) which results having higher energy contributions at low subspace dimensions. This analysis shows that the pressure distribution still has a dominant line shape in the first subspace dimension with small contributions from the second mode and supports the idea that it is representative of the ductile load build-up on the structure. As the subspace dimension increases, the contribution of higher order modes decreases. The second POM resemble to standing wave type of response that is active in the system, which illustrates the dynamic variation of the second POM. This result is consistent with the previous findings regarding the intermittent crushing in the DIIV test campaign where the most dominant mode resembles to line shape and second mode resembles to standing wave type response. Similarly, since the contribution of the higher order modes are very small, therefore negligible and do not have a specific physical meaning. However, one key difference between IVOS tests and the DIIV tests is that ice speed is lower in IVOS tests and kept constant during the test whereas it is increased stepwise in DIIV.

6. Discussion

Significant observations may be made from the use of these multivariate analyses in IIVs. It is showed that both methods (POD and IRPCA) can successfully identify the underlying fluctuating phenomena in ice-induced vibrations in intermittent crushing regime. However, as the ice speed is increased the quality of the reconstruction decreases due to the randomness in the phenomenon.

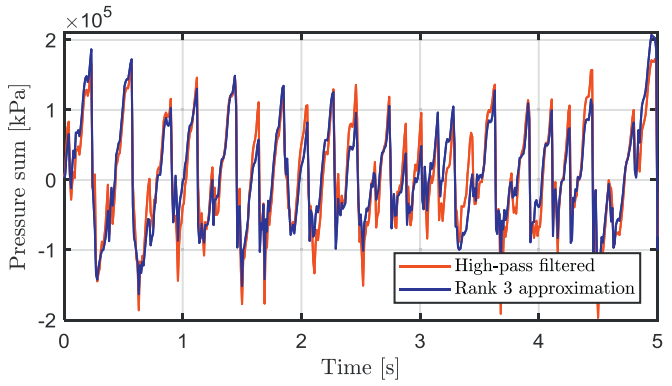

Fig. 10. Example time history of the sum of pressures for the original data (red) and rank-3 approximation (blue) at 60 *mm* s^{-1} ice speed obtained using IRPCA algorithm. (For interpretation of the references to colour in this figure legend, the reader is referred to the web version of this article.)

6.1. On the significance of the methods

Consider the traditional POD method first. It is shown that resulting eigenvalues in the POD analysis decay slowly after certain points, which suggests that there might be a lot of randomness, noise and/or corrupted data present and these prevent to form a good reduced-order model. For that reason, in order to evaluate the accuracy of these methods, NRMSE and theoretical minimal error analysis are used. The NRMSE percentage is computed between two signals (original and rank-3 approximated signals), and in theoretical error analysis eigenvalues are used as in Eq. (8). If the results of these two methods yield similar accuracy, this would be called an ideal error bound. However, this is not the case for the current dataset. For example, at 20 *mm* s^{-1}, the eigenvalue distribution suggests that the reconstruction of the original data using rank-3 approximation is possible with 49% accuracy if traditional POD analysis is used. However, if the signal reconstruction is considered and the NRMSE of rank-3 approximation is evaluated, it is found that original data is actually represented with 96% accuracy. In other words, distribution of the eigenvalues suggest that one need first 50 modes to get close to 96% accuracy, which in fact, it is only needed first three modes. Similar cases are observed at different ice speeds as well. The reason of this significant difference lies in the fundamental assumptions of POD: 1) linearity and 2) larger eigenvalues represent coherent structures. Although these assumptions generally believed to be true, sometimes it can be quite misleading and miss obvious facts. In fact, Kutz (2013) emphasizes this problem and illustrates that if the data includes large noise or outliers, it affects the results significantly where the decomposed modes are highly perturbed from their ideal states.

If we have large outliers in a data matrix, then POD will result a large bias, which will shift the true fit to compensate the outliers in the system. However, Candes and Wakin (2008) and Candes et al. (2011) showed that finding an $\mathcal{L}_1$-norm minimization solution to this data effectively rejects these outliers and robustifies the best data fit. This is

Table 3
(a) Test matrix, (b) modal energies for low-rank approximations of the matrices *L* and *A* for IRPCA and POD, respectively.

(a) Test-22,120		(b)	POD *E*[%] of A	IRPCA *E*[%] of L
f_n (*Hz*)	5.7	Rank 1	23	38
Diameter (*mm*)	200	Rank 2	41	65
Analyzed ice speed (*mm* s^{-1})	5	Rank 3	48	73
Sampling frequency (*Hz*)	300	Rank 10	65	89
Ice thickness (mm)	81	Rank 20	76	95
		Rank 50	90	99.9

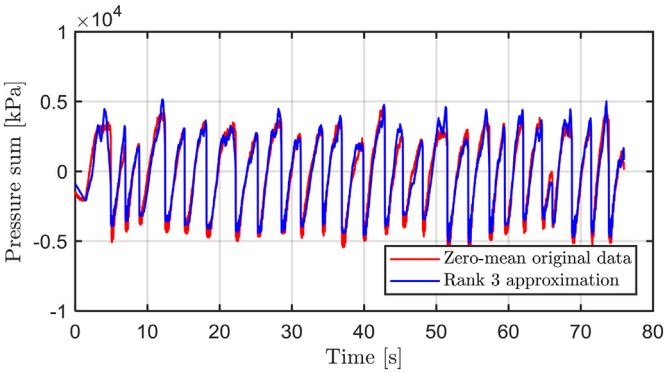

Fig. 12. Example time history of the sum of pressures for the zero-mean original data (red) and rank-3 approximation (blue) at 5 *mm* s^{-1} ice speed obtained using IRPCA algorithm. (For interpretation of the references to colour in this figure legend, the reader is referred to the web version of this article.)

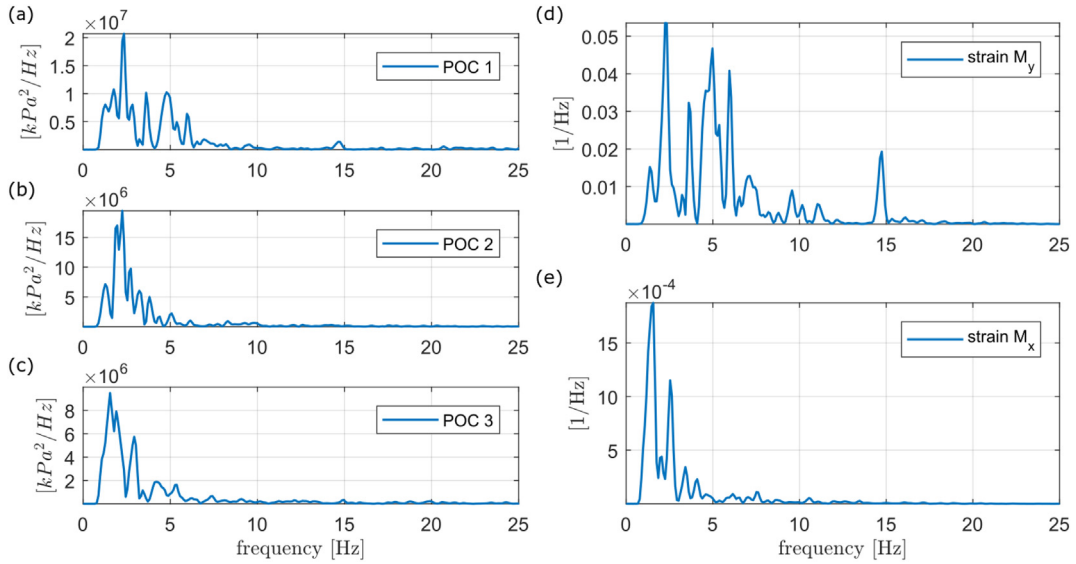

Fig. 11. Spectral densities of POD coefficients for the first three pressure modes (left) and spectral densities of strains due to ice action in the ice-drift direction (upper right) and sideways direction (lower right) at ice speed of 60 *mm* s^{-1}.

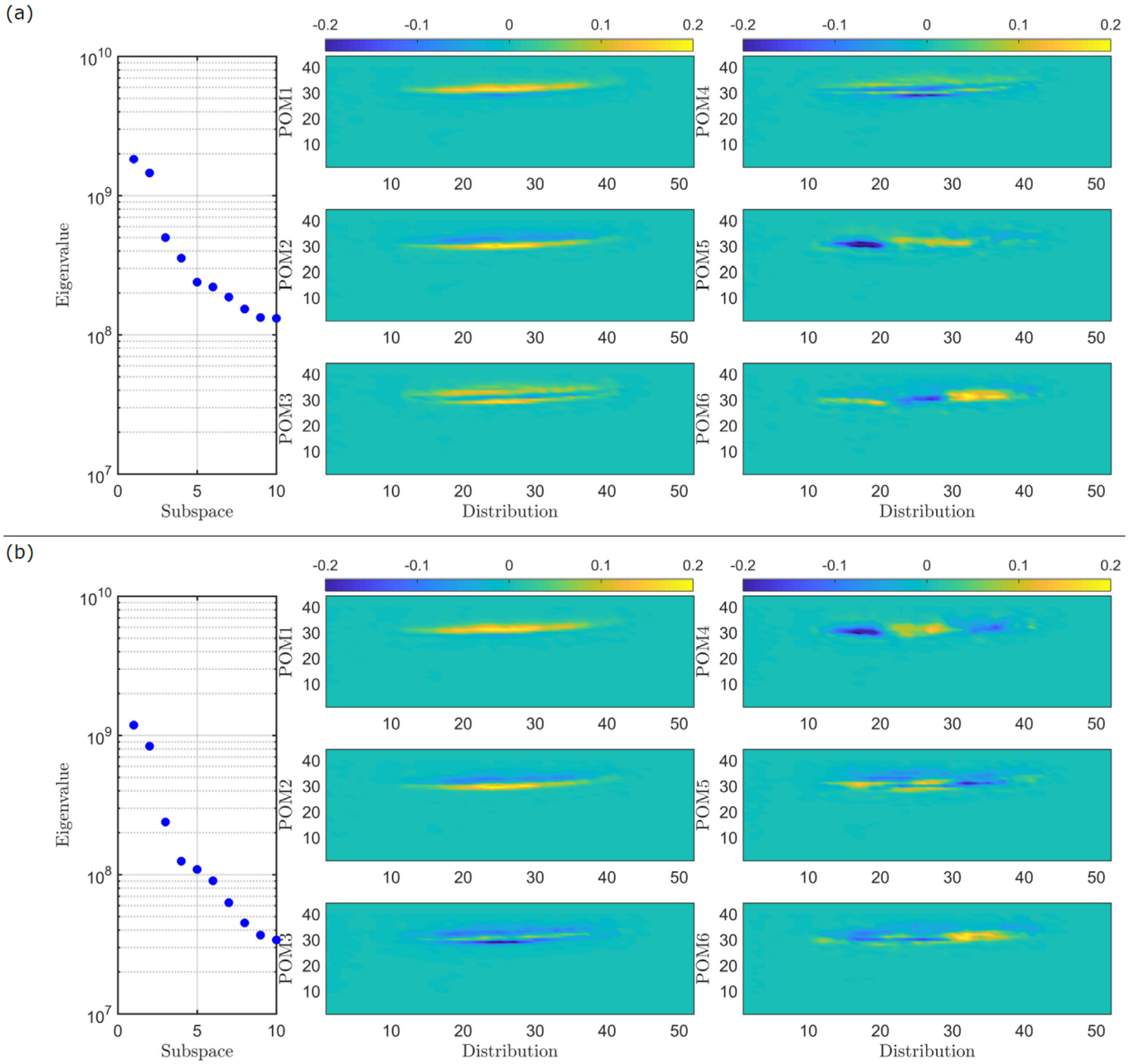

Fig. 13. Top image (a): Logarithmic plot of eigenvalues (left image) and corresponding six pressure modes (center and right images) at 5 $mm\ s^{-1}$ ice speed using POD. Bottom image (b): Logarithmic plot of eigenvalues (left image) and corresponding six pressure modes (center and right images) at 5 $mm\ s^{-1}$ ice speed using IRPCA.

significant, because if the data is corrupted, or has large noise embedded in it, then POD algorithm will potentially square the error and give misleading results. In that sense, $\mathscr{L}_1$-norm minimization promotes sparsity as illustrated in compressive sensing applications (see Candes and Wakin, 2008). For these reasons, in addition to traditional POD method, the IRPCA algorithm proposed by Lin et al. (2013) is also used to obtain the pressure modes. In this method, possible noise and/or corrupted data are separated from the original data and then POD is applied to the remaining low-rank data matrix. By using this method, the quality of the reconstruction from eigenvalues increases significantly as expected and this advanced treatment has minimal impact on the signal reconstruction of rank-3 approximation. In other words, the gap between the NRMSE and theoretical error analysis is decreased significantly. Another important point here is that, the regulating parameter λ is chosen to be constant for all the ice speeds to be consistent with the previous studies as suggested by Wright et al. (2009). However, Kutz (2013) also suggests that this parameter can be tuned to best separate the low-rank matrices from sparse components for better results. In fact, different λ values are tried in this study to see the effect of λ on the results, and it is observed that as λ is decreased to a certain point, the eigenvalues at lower subspace dimensions get larger but it makes the reconstruction of the data worse and vice versa. Although it is not shown, this suggests that an optimum λ value can be found that minimizes the probabilistic error between the error obtained from signal reconstruction and error obtained from the theoretical approach.

6.2. On the pressure modes

The methods used in this study demonstrate that it is effective to use

the subspaces of the spatially and temporally decomposed data to better understand ice-structure interactions. The methodology extracts the most important features necessary to reconstruct the original data with a tolerable accuracy. For ice-structure interaction on this structure, it is obvious that the first POM contributes in the same direction as the ice drift and has a shape similar to what is usually observed during the load build-up phase (Sodhi, 2001). Pressures that cause sideways motion of the structures are always observed in the second or third subspaces.

Sideway motions and their relationship to the pressure variations are compared using the frequency of the individual POCs and the frequency of the sideway motions. It is found that depending on the ice speed, frequency of the sideways motion coincides with the frequency of different POCs. This feature itself illustrates the complexity of the motion as a canonical problem. Without such a decomposition, it is difficult to distinguish between closely separated frequencies and understand their relationship to the structural motions. In particular, in the examples used in this study the sideway stiffness of the structure is lower than in the ice-drift direction, hence the frequency of the sideways motion in both cases are lower than in the ice-drift direction. In addition, Figs. 7 and 11 show that the magnitude of sideways motion is around three to four orders of magnitude lower than that in ice-drift direction. Therefore, with classical frame by frame inspection, it is difficult to distinguish the sideways motion from the ice-drift directed motion, especially when their dominant frequencies are close. Any change in ice parameters may lead to other subsets of POMs that can be used to better model ice-structure interactions. This is very important because sideways motion of the structure also occur in full-scale (Nord et al., 2016), therefore the effect of pressure modes on the sideway motion need to be further investigated to understand this complex phenomenon better.

Although good results are achieved for intermittent crushing, the error increases with the ice speed. The physical explanation of that is twofold. At higher ice speeds, brittle failure of ice over small regions during continuous crushing increases which leads loss of coherence in pressure modes. When the tactile sensor measures frames at a frequency of 100 Hz, only $2-3$ frames of pressure are recorded during brittle failure, which makes it difficult to extract coherent structures from the data. Because of this limitation in the sensor, continuous brittle crushing and frequency lock-in are intentionally left out of the analysis.

7. Conclusion

In conclusion, this study illustrates the complex nature of ice-induced vibrations. The purpose of this study is to illustrate the systematic pressure distributions hidden in ice-induced vibrations to have a better understanding of the phenomenon. Being able to clearly identify pressure modes that are active in the ice-structure interaction is of utmost importance to the development of the reduced-order models capable of predicting ice-induced vibrations in offshore structures. For that purpose, authors apply POD and IRPCA methods to the selected datasets to examine the pressure activities. Active pressure modes in the system are compared along with their contributions using NRMSE and theoretical error analysis. Physical meaning of the pressure modes are interpreted for the selected ice speeds.

As a result of the analyses, it is found that first pressure mode illustrates the ductile pressure variation on the structure which is the most dominant mode and inherently varies in the direction of ice drift. It is also showed that some combination of first three pressure modes represent the oscillations in the sideways direction of the structure. It is hypothesized that higher order modes are contaminated with some added noise due to complex ice-structure interaction.

In addition to obtaining the pressure modes, it is also shown that the coordinate system employed using IRPCA for reduced order modeling is more efficient and robust than POD, and can greatly reduce the amount of data that needs to be stored that faithfully represents the original dataset. For example, as Table 2 shows, regardless of the ice speed analyzed, one can reconstruct the original data using first 50 subspaces without losing any information.

It is important to note that, the intention of this work is not to favor one method over another. It is also only applied to several ice speeds in the intermittent crushing type of failure hence cannot be generalized. However, if one needs to characterize the pressure modes for all the ice speeds and different type of failure modes, a more detailed extensive study is needed. In fact, it is known that other multivariate analysis methods such as smooth-orthogonal decomposition (Chelidze and Zhou, 2006; Gedikli et al., 2017; Gedikli et al., 2018a, 2018b), or dynamic mode decomposition (Tu, 2013) demonstrated to work better in highly nonlinear systems. However, POD and IRPCA methods are used in this work for clarity as a first step analyzing ice-induced vibration dataset using multivariate analysis.

Acknowledgement

The work described in this paper was supported by the European Community's 7th Framework Program through the grant to the budget of the Integrated Infrastructure Initiative HYDRALAB-IV, Contract no. 261520. The authors would like to thank the Hamburg Ship Model Basin (HSVA), especially the ice tank crew, for the hospitality, technical and scientific support and the professional execution of the test program in the Research Infrastructure ARCTECLAB.

References

Barker, A., Timco, G., Gravesen, H., Vølund, P., 2005. Ice loading on Danish wind turbines: part 1: dynamic model tests. Cold Reg. Sci. Technol. 41 (1), 1–23.
Berkooz, G., Holmes, P., Lumley, J.L., 1993. The proper orthogonal decomposition in the analysis of turbulent flows. Annu. Rev. Fluid Mech. 25 (1), 539–575.
Bjerkås, M., Alsos, H.S., Meese, A., 2013. Ice Induced Vibrations - Observations of a Full Scale Lock-in Event, The Twenty-third International Offshore and Polar Engineering Conference. International Society of Offshore and Polar Engineers, Anchorage, Alaska.
Blenkarn, K.A., 1970. Measurement and Analysis of Ice Forces on Cook Inlet structures, Offshore Technology Conference. Offshore Technology Conference, Houston, Texas.
Candes, E.J., Wakin, M.B., 2008. An introduction to compressive sampling. IEEE Signal Process. Mag. 25 (2), 21–30.
Candes, E.J., Li, X., Ma, Y., Wright, J., 2011. Robust principal component analysis? J. ACM 58 (3), 1–37.
Chatterjee, A., 2000. An introduction to the proper orthogonal decomposition. Curr. Sci. 78 (7), 808–817.
Chelidze, D., Zhou, W., 2006. Smooth orthogonal decomposition-based vibration mode identification. J. Sound Vib. 292 (3), 461–473.
Cruz, A.S., David, L., Pécheux, J., Texier, A., 2005. Characterization by proper-orthogonal-decomposition of the passive controlled wake flow downstream of a half cylinder. Exp. Fluids 39 (4), 730–742.
Epps, B.P., Techet, A.H., 2010. An error threshold criterion for singular value decomposition modes extracted from PIV data. Exp. Fluids 48 (2), 355–367.
Feeny, B.F., Kappagantu, R., 1998. On the physical interpretation of proper orthogonal modes in vibrations. J. Sound Vib. 211 (4), 607–616.
Frederking, R.M.W., Haynes, F.D., Hodgson, T.P., Sayed, M., 1986. Static and dynamic ice loads on the Yamachiche Bend lightpier, 1984–86. vol. 3. pp. 115–126.
Gagnon, R.E., 1994. Generation of melt during crushing experiments on freshwater ice. Cold Reg. Sci. Technol. 22 (4), 385–398.
Gedikli, E.D., Dahl, J.M., 2017. Mode excitation hysteresis of a flexible cylinder undergoing vortex-induced vibrations. J. Fluids Struct. 69, 308–322.
Gedikli, E., Dahl, J., Chelidze, D., 2017. Multivariate analysis of vortex-induced vibrations in a tensioned cylinder reveal nonlinear modal interactions. Procedia Eng. 199 (Supplement C), 546–551.
Gedikli, E.D., Chelidze, D., Dahl, J.M., 2018a. Bending Dominated Flexible Cylinder Experiments Reveal Insights into Modal Interactions for Flexible Body Vortex-Induced Vibrations, The 28th International Ocean and Polar Engineering Conference. International Society of Offshore and Polar Engineers.
Gedikli, E.D., Chelidze, D., Dahl, J.M., 2018b. Observed mode shape effects on the vortex-induced vibration of bending dominated flexible cylinders simply supported at both ends. J. Fluids Struct. 81, 399–417.
Joensuu, A., Riska, K., 1988. Ice-Structure Contact, Report M88. ISBN 951-754-773-0. Helsinki University of Technology, Faculty of Mechanical Engineering, Laboratory of Naval Architecture and Marine Engineering.
Jordaan, I.J., 2001. Mechanics of ice–structure interaction. Eng. Fract. Mech. 68 (17), 1923–1960.
Kärnä, T., Kolari, K., Jochmann, P., Evers, K.-U., Bi, X., Määttänen, M., Martonen, P., 2003. Tests on Dynamic Ice-Structure Interaction. vol. 36835. pp. 823–829.
Kärnä, T., Kolari, K., Jochmann, P., Evers, K.-U., Bi, X., Määttänen, M., Martonen, P., 2003b. Ice Action on Compliant Structures. VTT Research Notes 2223. VTT.

Kerschen, G., Golinval, J.-c., Vakakis, A.F., Bergman, L.A., 2005. The method of proper orthogonal decomposition for dynamical characterization and order reduction of mechanical systems: an overview. Nonlinear Dyn. 41 (1), 147–169.
Kutz, N., 2013. Data-Driven Modeling and Scientific Computation. Oxford University Press.
Lin, Z., Chen, M., Ma, Y., 2013. The Augmented Lagrange Multiplier Method for Exact Recovery of Corrupted Low-Rank Matrices. UIUC Technical Report (arXiv:1009.5055v3).
Ma, X., Vakakis, A.F., Bergman, L.A., 2001. Karhunen-Loe`ve modes of a truss: transient response reconstruction and experimental verification. AIAA J. 39 (4), 687–696.
Määttänen, M., 1975. Experiences of ice forces against a steel lighthouse mounted on the seabed, and proposed constructional refinements. In: Port and Ocean Engineering Under Arctic Conditions (POAC), Fairbanks, Alaska, pp. 857–867.
Määttänen, M., Marjavaara, P., Saarinen, S., Laakso, M., 2011. Ice crushing tests with variable structural flexibility. Cold Reg. Sci. Technol. 67 (3), 120–128.
Määttänen, M., Løset, S., Metrikine, A., Evers, K.-U., Hendrikse, H., Løney, C., Metrikin, I., Nord, T.S., Sukhorukov, S., 2012. Novel Ice Induced Vibration Testing in a Large-Scale Facility, 21st IAHR International Symposium on Ice. Ice Research for a Sustainable Environment, Dalian, China.
Nord, T.S., Lourens, E.-M., Määttänen, M., Øiseth, O., Høyland, K.V., 2015. Laboratory experiments to study ice-induced vibrations of scaled model structures during their interaction with level ice at different ice velocities. Cold Reg. Sci. Technol. 119, 1–15.
Nord, T.S., Øiseth, O., Lourens, E.-M., 2016. Ice force identification on the Nordströmsgrund lighthouse. Comput. Struct. 169, 24–39 Supplement C.
O'Rourke, B.J., Jordaan, I.J., Taylor, R.S., Gürtner, A., 2016a. Experimental investigation of oscillation of loads in ice high-pressure zones, part 1: single indentor system. Cold Reg. Sci. Technol. 124, 25–39.
O'Rourke, B.J., Jordaan, I.J., Taylor, R.S., Gürtner, A., 2016b. Experimental investigation of oscillation of loads in ice high-pressure zones, part 2: double indentor system — coupling and synchronization of high-pressure zones. Cold Reg. Sci. Technol. 124, 11–24.
Sodhi, D.S., 2001. Crushing failure during ice–structure interaction. Eng. Fract. Mech. 68 (17–18), 1889–1921.
Sodhi, D., Haehnel, R., 2003. Crushing ice forces on structures. J. Cold Reg. Eng. 17 (4), 153–170.
Tu, J., 2013. Dynamic Mode Decomposition: Theory and Applications Princeton University.
Wells, J., Jordaan, I., Derradji-Aouat, A., Taylor, R., 2011. Small-scale laboratory experiments on the indentation failure of polycrystalline ice in compression: main results and pressure distribution. Cold Reg. Sci. Technol. 65 (3), 314–325.
Wright, J., Ganesh, A., Rao, S., Peng, Y., Ma, Y., 2009. Robust Principal Component Analysis: Exact Recovery of Corrupted Low-Rank Matrices by Convex Optimization. NIPS Proceedings.
Ziemer, G., Hinse, P., 2017. Relation of Maximum Structural Velocity and Ice Drift Speed during Frequency Lock-In, Proceedings of the 24th International Conference on Port and Ocean Engineering under Arctic Conditions, Busan, Korea.